Amino Acid Residues His183 and Glu264 in *Bacillus subtilis* Ferrochelatase Direct and Facilitate the Insertion of Metal Ion into Protoporphyrin IX[†,‡]

Mattias D. Hansson,*[,§,||] Tobias Karlberg,[||,⊥] Muhammad Arys Rahardja,[§] Salam Al-Karadaghi,[⊥] and Mats Hansson[§]

Department of Biochemistry and Department of Molecular Biophysics, Lund University, Box 124, 221 00 Lund, Sweden

Received August 25, 2006; Revised Manuscript Received October 28, 2006

ABSTRACT: Ferrochelatase catalyzes the terminal step in the heme biosynthetic pathway, i.e., the incorporation of Fe(II) into protoporphyrin IX. Various biochemical and biophysical methods have been used to probe the enzyme for metal binding residues and the location of the active site. However, the location of the metal binding site and the path of the metal into the porphyrin are still disputed. Using site-directed mutagenesis on *Bacillus subtilis* ferrochelatase we demonstrate that exchange of the conserved residues His183 and Glu264 affects the metal affinity of the enzyme. We also present the first X-ray crystal structure of ferrochelatase with iron. Only a single iron was found in the active site, coordinated in a square pyramidal fashion by two amino acid residues, His183 and Glu264, and three water molecules. This iron was not present in the structure of a His183Ala modified ferrochelatase. The results strongly suggest that the insertion of a metal ion into protoporphyrin IX by ferrochelatase occurs from a metal binding site represented by His183 and Glu264.

Ferrochelatase (E.C. 4.99.1.1) catalyzes the insertion of Fe(II) into protoporphyrin IX. This is the final reaction in the heme biosynthetic pathway (*1*). Heme participates in many essential cellular functions, e.g., in the respiratory chain and in the transport of oxygen, and it is crucial for most organisms (*2*, *3*). Deficiency of ferrochelatase in humans leads to the accumulation of free protoporphyrin in the erythrocytes and a lifelong photosensitive condition called erythropoietic protoporphyria (*4*). This phototoxic property is however utilized in cancer therapy. Tumor cells are induced to accumulate protoporphyrin, which leads to cell necrosis after treatment with light (*5*, *6*). These examples show that understanding the ferrochelatase reaction mechanism is of common interest.

The ferrochelatase reaction has also been mimicked by catalytic antibodies (*7*, *8*), RNA (*9*), and DNA (*10*) as a model system to promote the understanding of catalytic processes. The reaction is a beautiful example of a stretch-and-bending mechanism as the porphyrin substrate is tilted out of the plane by ferrochelatase (*11*). The distortion of the macrocycle exposes the pyrrole nitrogen to the incoming metal substrate, which allows the first metal−porphyrin bond to be formed, as recently reviewed by Al-Karadaghi et al. (*12*). Interestingly, the metal specificities vary for ferrochelatases purified from different sources. *Bacillus subtilis* ferrochelatase can, in addition to Fe(II), incorporate Cu(II) and Zn(II) ions into porphyrins *in vitro* (*13*). Generally, ferrochelatases from other organisms do not incorporate Cu(II). In contrast, Zn(II) is incorporated into porphyrin by all characterized ferrochelatases and it has commonly been used in assays as the aerobic sensitivity of Fe(II) makes it difficult to use (*14*). Zn(II) ions commonly antagonize Fe(II)- and Cu(II)-dependent catalytic activity, presumably by competing for the metal binding site (*15*). The major role of ferrochelatase in accelerating the reaction with regard to the metal substrate has been suggested to include dehydration and an increase in the ligand exchange rate of the metal (*16*, *17*). The abstraction of protons from the porphyrin is also essential for catalysis. This has been suggested to take place after the formation of the first metal−nitrogen bond (*18*).

Over the past decade determination of the position of the catalytic metal binding site in ferrochelatase has been within the focus of several research groups. Extensive site-directed mutagenesis studies have been used to probe for and identify the metal binding site (*19*−*21*). In these studies, estimates of the roles of various amino acid residues in metal binding have always been based on activity measurements instead of direct measurements of metal affinity.

X-ray crystal structures of ferrochelatase from three different organisms have been solved: from *B. subtilis* (*22*), *Homo sapiens* (*23*), and *Saccharomyces cerevisiae* (*24*). All structures displayed two similar domains with a Rossmann-type of fold. The same fold was also found in the anaerobic cobalt chelatase from *Salmonella typhimurium* (*25*). This led to the suggestion that the two chelatases constitute a class of tetrapyrrole chelatases with similar reaction mechanisms. Even though various divalent metal ions such as Zn(II), Cu(II), Co(II), Cd(II), and Hg(II) have been observed in X-ray crystallographic structures of ferrochelatases, none of the solved structures have contained the metal substrate Fe(II). Metal binding has also been characterized using methods such as Mössbauer spectroscopy (*26*) and extended

[†] This work was supported by The Swedish Research Council (to M.H. and S.A-K.) and The Crafoord Foundation (to M.H.).

[‡] The coordinates have been deposited within the Protein Data Bank (PDB codes 2HK6, 2H1W, and 2H1V).

* To whom correspondence should be addressed. Tel: +46 46 2220278. Fax: +46 46 2224116. E-mail: mattias.hansson@biochemistry.lu.se.

[§] Department of Biochemistry.

[||] The authors contributed equally to the work.

[⊥] Department of Molecular Biophysics.

10.1021/bi061760a CCC: $37.00
Published on Web 12/08/2006

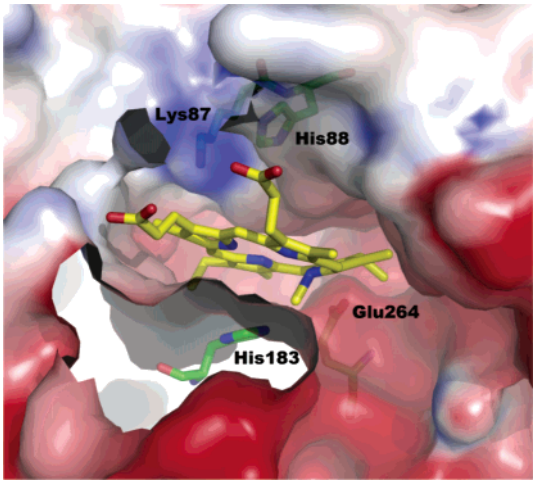

FIGURE 1: Amino acid residues in the porphyrin binding cleft of *B. subtilis* ferrochelatase displaying the two suggested entrances for the metal ion into protoporphyrin IX. The electrostatic surface potential is shown, red being negative and blue positive. The final metal binding site prior to porphyrin incorporation is formed either by the conserved residues His183 and Glu264 below the porphyrin or by the nonconserved Lys87 and His88 above it. The figure was prepared with PyMOL (*47*).

X-ray absorption fine structure (EXAFS)[1] (*27*). Two alternative sites for metal binding prior to porphyrin incorporation have been considered. The first site, which involves the conserved residues His183 and Glu264 (*B. subtilis* numbering), is located inside the porphyrin binding cleft in close vicinity to the tilted pyrrole of the inhibitor *N*-methylmesoporphyrin (*N*-MeMP) (*28*). The second site, which is located on the opposite side of the bound porphyrin, has been suggested to involve the nonconserved residues His88 and Lys87 (*B. subtilis* numbering) (*21*) (Figure 1).

In this paper we present direct estimates of metal affinity for a series of modified ferrochelatases: His183Ala, His183Cys, Glu264Val, Glu264Gln, Tyr13Phe, His88Ala, and Lys87Ala. We also present the first structure of ferrochelatase in complex with iron at 1.7 Å resolution. The results strongly favor a path where the metal ion is inserted into protoporphyrin IX via the conserved residues His183 and Glu264.

EXPERIMENTAL PROCEDURES

Mutagenesis. Mutations corresponding to His183Ala, Glu264Val, Glu264Gln, His88Ala, and Lys87Ala replacements were introduced into ferrochelatase by the QuikChange method (Stratagene) using *Pfu* DNA polymerase (Fermentas) and a PTC-200 Peltier Thermal Cycler (MJ Research). Plasmid pLUGT7-H containing the *B. subtilis hemH* ferrochelatase gene was used as a template (*29*). The following primers were used: H183Aup 5′-CAATGCT**C**ATCGTATCTGCAGCCAGCCTGCCGGAAAAAATC-3′; H183Adown 5′-GATTTTTTCCGGCAGGCTGGCTGCAGATACGATGAGCATTG-3′; E264Va 5′-ATTATCATAAAGCACTACTAAGTGATC-3′; E264Qa 5′-ATTATCATAAAGCACTTGTAAGTGATC-3′; H88Afor 5′-GAGATTACGTTTAAGGCGTATATCGGACTGAAGGCTATCGAGCC-3′; H88Arev 5′-GGCTCGATAGCCTTCAGTCCGATATACGCCTTAAACGTAATCTC-3′; K87Afor 5′-GAGATTACGTTTAAGGCGTATATCGGACTGGCGCATATCGAGCC-3′; K87Arev 5′-GGCTCGATATGCGCCAGTCCGATATACGCCTTAAACGTAATCTC-3′. Introduced mismatches are underlined. The introduced mutations were confirmed in plasmids pH183A, pE264V, pE264Q, pH88A, and pK87A by DNA sequencing of the entire *hemH* gene. Plasmids encoding *B. subtilis* ferrochelatase with either a His183Cys or a Tyr13Phe modification have previously been constructed (*17*). The bacterial strains and plasmids used in the present work are listed in Table 1.

Table 1: Bacterial Strains and Plasmids

strain or plasmid	genotype or description	ref
strain		
E. coli BL21(DE3)	*hsdS gal* (λ*c*I*ts*857 *ind1 Sam1 nin5 lacUV5*-T7 *gene 1)*	*46*
plasmids		
pLUGT7-H	*bla*; *B. subtilis hemH* cloned downstream of the T7 promoter of pBluescript II KS(−), template for mutagenesis	*29*
pH183A	pLUGT7-H derivative. C-to-T silent point mutation in bp 544 and CA-to-GC point mutations in bp 547 and 548 of the *B. subtilis hemH*	*a*
pH183C	pLUGT7-H derivative. CA-to-TG point mutations in bp 547 and 548 of the *B. subtilis hemH*	*17*
pE264V	pLUGT7-H derivative. A-to-T point mutation in bp 791 of the *B. subtilis hemH*	*a*
pE264Q	pLUGT7-H derivative. G-to-C point mutation in bp 790 of the *B. subtilis hemH*	*a*
pY13F	pLUGT7-H derivative. A-to-T point mutation in bp 38 of the *B. subtilis hemH*	*17*
pH88A	pLUGT7-H derivative. A-to-G silent point mutation in bp 243 and CA-to-GC point mutations in bp 262 and 263 of the *B. subtilis hemH*	*a*
pK87A	pLUGT7-H derivative. A-to-G silent point mutation in bp 243 and AA-to-GC point mutations in bp 259 and 260 of the *B. subtilis hemH*	*a*

[a] Present work.

Protein Preparation, Activity, and K_d Measurements. The wild-type and modified *B. subtilis* ferrochelatases were expressed in *Escherichia coli* BL21(DE3) and purified from inclusion bodies as described by Hansson et al. (*30*). Activity measurements and K_d estimations were also performed according to the same reference (*30*). Grubbs' test based on the residuals was used to identify outliers in the Zn(II) titrations of the protein. Between three and six series of titrations were performed for each ferrochelatase variant. Each titration was independently plotted, and the K_d was estimated using the software GraphPad Prism (*31*). A Student's *t*-test identified the modified ferrochelatases that displayed significantly different K_d values.

Circular Dichroism Spectroscopy. The circular dichroism (CD) spectra were obtained using a Jasco J-720 spectropolarimeter with a Jasco PTC-343 Peltier type thermostatic cell holder. All data were collected at 25.0 °C. Only data for which the voltage of the photomultiplier was below 700 V were used. At voltages above 700 V, the photomultiplier of the instrument becomes saturated and the signal-to-noise ratio of the CD signal deteriorates rapidly. Hence, the lower wavelengths were excluded due to high absorbance.

Crystallization, Data Collection, and Refinement. Initial crystals of His183Ala and Lys87Ala modified ferrochelatases

[1] Abbreviations: EXAFS, extended X-ray absorption fine structure; *N*-MeMP, *N*-methylmesoporphyrin; CD, circular dichroism; ADP, anisotropic displacement parameters; rmsd, root-mean-square deviations.

Table 2: Data Collection and Refinement Statistics for Wild-Type and His183Ala Ferrochelatase Crystals Soaked with Fe and for Ferrochelatase with a Lys87Ala Modification

	wild-type:Fe	His183Ala:Fe	Lys87Ala
data collection			
beamline	I711	I911-3	I911-2
wavelength (Å)	1.0605	1.0000	1.00754
cell dimensions[a]			
a (Å)	48.65	47.95	47.70
b (Å)	49.98	49.71	49.40
c (Å)	118.85	116.53	117.20
resolution range (Å)	20.0−1.70	19.5−2.60	25.0−1.20
completeness (%)	99.0	95.8	93.9
no. of unique reflns	59900	16160	83273
multiplicity	11.3	3.8	5.1
$I/\sigma(I) > 3$ (%)	95.4	89.4	91.1
R_{merge} (%)[b]	2.7	12.3	6.7
in the highest-resolution shell			
resolution range (Å)	1.81−1.70	2.76−2.60	1.27−1.20
completeness (%)	84.8	91.8	70.2
$I/\sigma(I) > 3$ (%)	79.9	64.9	67.2
R_{merge} (%)[b]	8.9	34.0	23.3
refinement			
no. of protein atoms	2495	2481	2587
no. of water molecules	368	7	468
no. of iron atoms	4	1	
R_{cryst} (R_{free})[c] (%)	17.8 (21.9)	21.8 (25.9)	12.3 (17.3)
mean *B* value (Å^2)	15.6	42.0	
rmsd[d]			
bond lengths (Å)	0.010	0.008	0.012
bond angles (deg)	3.2	1.2	3.0

[a] Space group $P2_12_12_1$. [b] $R_{merge} = \sum|I_i - \langle I\rangle|/\sum I$, where I_i is an individual intensity measurement and $\langle I\rangle$ is the average intensity for this reflection. [c] $R_{cryst} = \sum|F_{obs} - F_{calc}|/\sum F_{obs}$, where F_{obs} and F_{calc} are the observed and calculated structure factor amplitudes, respectively. R_{free} is the same as R_{cryst} but calculated on 5% of the data excluded from refinement. [d] Root-mean-square deviations of the parameters from their ideal values.

were found by screening around wild-type crystallization conditions. The initial crystals were further optimized by employing seeding techniques as described by Hansson et al. (*29*). Soaking was conducted by transferring a crystal to a drop containing 10 μL of well solution, adding one $(NH_4)_2Fe(SO_4)_2\cdot 6H_2O$ salt crystal, and incubating for 35 min. During this time period the salt crystal dissolved completely. After soaking, the ferrochelatase crystal was transferred to another drop containing well solution prepared with 10% PEG 400 as a cryoprotectant. A nylon loop was used to mount the crystal and flash-freeze it in a stream of boiled off nitrogen. Data for a wild-type ferrochelatase crystal soaked in Fe was collected at beamline I711, whereas for crystals of the His183Ala and Lys87Ala variants, data were collected at beamlines I911-3 and I911-2 respectively, at the MAX II synchrotron radiation facility in Lund, Sweden (*32*−*34*). All data were indexed and integrated in space group $P2_12_12_1$ with the XDS package (*35*).

The structures were refined using CNS (*36*) and SHELXL-97 (*37*) software packages. The models were built using the graphical program O (*38*). For the ferrochelatase with a Lys87Ala modification, which diffracted to 1.2 Å resolution, a total of 12 side chains were modeled in alternate conformations. The progress of refinement was followed by decreasing *R* and R_{free} values. Data collection and refinement statistics are presented in Table 2. Coordinates for the crystal structure were deposited in the Protein Data Bank, accession codes 2HK6 (wild-type:Fe), 2H1W (His183Ala:Fe), and 2H1V (Lys87Ala).

Table 3: Activity and K_d of Wild-Type and Modified Ferrochelatases

	activity (%)	K_d (μM)	*P*[a]
wild-type	100 ± 9	3.7 ± 0.4[b]	
His183Ala	<1	15 ± 1	<0.01
His183Cys	<1	0.64 ± 0.06	<0.01
Glu264Val	<1		
Glu264Gln	21 ± 3	3.7 ± 1.8	>0.05
Tyr13Phe	71 ± 4	4.8 ± 2.6	>0.05
His88Ala	5 ± 1	2.8 ± 0.4	>0.05
Lys87Ala	92 ± 17	13 ± 5	<0.01

[a] *P* represents the probability when comparing the K_d of the modified ferrochelatase to the wild-type enzyme using a Student's *t*-test. [b] From ref *30*.

Estimating Intrinsic pK_a Values. Calculations of intrinsic pK_a values were performed with the AMBER 8 force field at pH 7.4 using the H++ server (*39*). The program uses the continuum electrostatic model to calculate titration curves and protonation states (*40*). Calculations were done by using coordinates from the PDB: 1DOZ (wild-type) and 2H1V (Lys87Ala).

RESULTS

Metal Binding to Modified Ferrochelatases. To identify the site important for metal binding during catalysis, amino acid residues on both sides of the porphyrin binding cleft were targeted for site-directed mutagenesis. The affinities for Zn(II) ions of the modified ferrochelatases were estimated by monitoring the dependence of intrinsic tryptophan fluorescence on the Zn(II) concentration. The same method has recently been used to estimate the K_d for Zn(II) binding to wild-type ferrochelatase (3.7 ± 0.4 μM) (*30*).

Replacing His183 with an alanine gave an almost inactive enzyme and a K_d for Zn(II) ions that was 15 ± 1 μM, i.e., a 4-fold decrease in affinity compared to wild-type enzyme (Table 3). To further validate the involvement of His183 in metal coordination, metal binding affinity was estimated for ferrochelatase with a His183Cys modification. Cysteines are commonly found as ligands in proteins in which zinc has a structural role (*41*). The sulfur of a cysteine is expected to bind Zn(II) tighter than the nitrogen of a histidine. The His183Cys modified ferrochelatase displayed a K_d of 0.64 ± 0.06 μM for Zn(II). This is an almost 6-fold increased affinity compared to the wild-type protein. High structural similarity to the wild-type enzyme (*11*, *17*) suggest that the tighter binding is the most probable reason for the low activity of the enzyme, which was less than 1% of wild-type. Thus, the change in metal affinity following the replacement of histidine by alanine and cysteine both gave a decrease in the activity of ferrochelatase. These results, together with earlier biochemical and structural data, strongly suggest that His183 is involved in metal binding during the ferrochelatase reaction.

B. subtilis ferrochelatase also appears to be sensitive to modifications of Glu264. In a Glu264Val modified ferrochelatase the maximum fluorescence intensity was reduced only by 8% upon Zn(II) titration. As a consequence, no reliable K_d could be estimated. The activity of this variant was also less than 1% of wild-type, which again suggests that a change in metal binding is followed by a low enzymatic activity. A ferrochelatase with a Glu264Gln

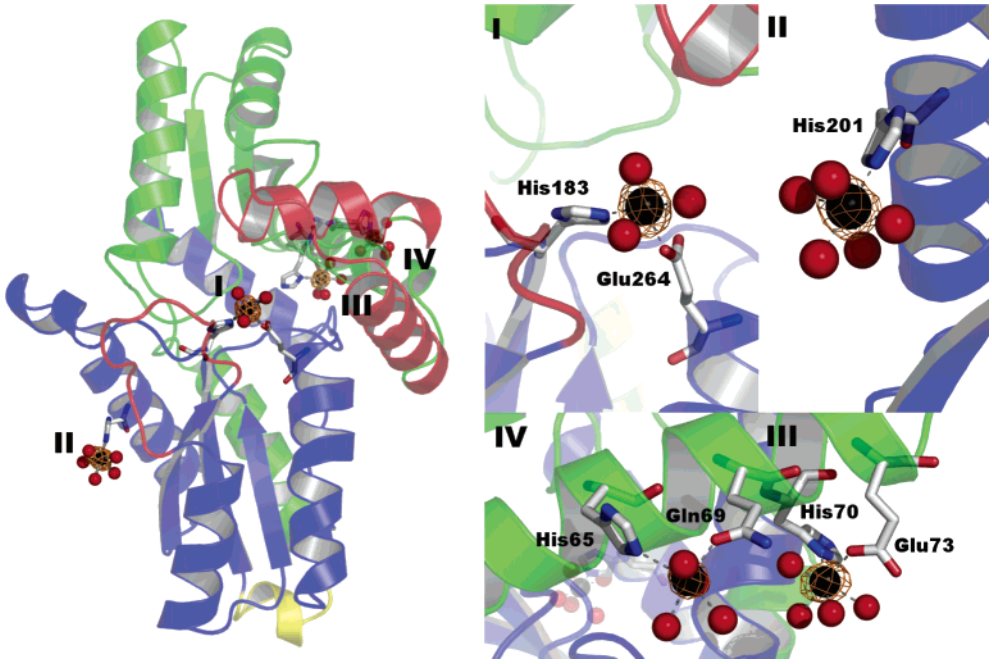

FIGURE 2: The four irons bound to *B. subtilis* ferrochelatase. The irons are shown as black spheres and waters as red. A calculated anomalous Bijvoet difference electron density map is shown in orange at the 5σ level. In the overall structure the domains are colored green and blue, the porphyrin binding cleft is red, and the linker region is yellow. The figure was prepared with PyMOL (*47*).

modification retained a relatively high activity, 21%. The estimated K_d was also 3.7 ± 1.8 μM, which is not significantly different from that of wild-type. This shows that the metal is still able to bind to this variant.

Apart from His183 and Glu264, the nonconserved Tyr13, His88, and Lys87 are three other polar residues located in close vicinity to the porphyrin. They are positioned on the opposite side of the porphyrin binding cleft compared to His183 and Glu264. Even though Tyr13 has not been proposed to function as a primary metal binding residue, it has been observed to serve as the second sphere ligand to Zn(II) in the absence of porphyrin (*28*). In most organisms Tyr13 is replaced by a methionine. However, in some bacteria, e.g., *Propionibacterium freudenreichii* (*42*) and *Mycobacterium tuberculosis* (*43*), it is replaced by phenylalanine. A Tyr13Phe replacement in *B. subtilis* ferrochelatase has not affected metal binding, i.e., Zn(II) has been observed bound in a wild-type fashion in the structure (*17*). Tyr13 has also been observed as an axial ligand for copper in the complex of Cu(II)−*N*-MeMP with wild-type ferrochelatase (*11*). In the present study, the K_d for Zn(II) ions of the Tyr13Phe variant was estimated to 4.8 ± 2.6 μM and the rate of incorporation of Zn(II) into protoporphyrin IX was only slightly affected by the modification.

From studies of human ferrochelatase, Sellers et al. (*21*) have suggested that the *B. subtilis* residues His88 and Lys87 form a metal binding site located in the upper part of the porphyrin binding cleft (Figure 1). The replacement of His88 by an alanine resulted in a K_d value of 2.8 ± 0.4 μM, which is close to that of the wild-type enzyme. This suggests that His88 is not involved in the coordination of the metal. However, enzyme activity was 5% of the wild-type ferrochelatase, suggesting that this residue is still important for the catalytic mechanism. The replacement of the second residue in this site, Lys87, by an alanine resulted in a ferrochelatase that retained 92% of wild-type activity, but had a K_d that was significantly higher than that of wild-type enzyme: 13 ± 5 μM.

Table 4: Residues Involved in the Coordination of Previously Observed Metal Ions Bound at the Active Site of Ferrochelatase

metal	ligands (Å)	coordination	ref
Zn(II)	His183 (2.13) Glu264 (2.22) Wat432 (1.96) Wat433 (2.30)	distorted tetrahedral	*28*
Cd(II)	His183 (2.41) Glu264 (2.65) Wat69 (2.68) Wat139 (2.89) Wat352 (3.11)	trigonal bipyramidal	*28*
Fe	His183 (2.18) Glu264 (2.20) Wat926 (1.80) Wat674 (2.15) Wat675 (2.32)	square pyramidal	*a*

[a] Present work.

Crystal Structures. Addition of solid $(NH_4)_2Fe(SO_4)_2 \cdot 6H_2O$ to a solution containing *B. subtilis* ferrochelatase crystals was a successful approach to obtain crystals of an Fe−ferrochelatase complex. In previous experiments, soaking procedures employing Fe(II) solutions were tried without success, whereas the gentle metal soaking procedure used in the present study did not seem to affect the crystal quality. Hence good diffraction data to 1.7 Å were collected (Table 2). Following this treatment, four irons were found in the ferrochelatase structure (Figure 2, Table 4). In the active site (I), one iron coordinated by His183, Glu264, and three water molecules in a square pyramidal fashion was observed. The same residues have been observed to be involved in zinc coordination, although in that case the metal coordination was distorted tetrahedral (*28*). In the second coordination sphere Tyr13 and Ser222 stabilize two of the water ligands. A higher temperature factor and weaker electron density of the water molecule bridging the iron and Tyr13 indicated a

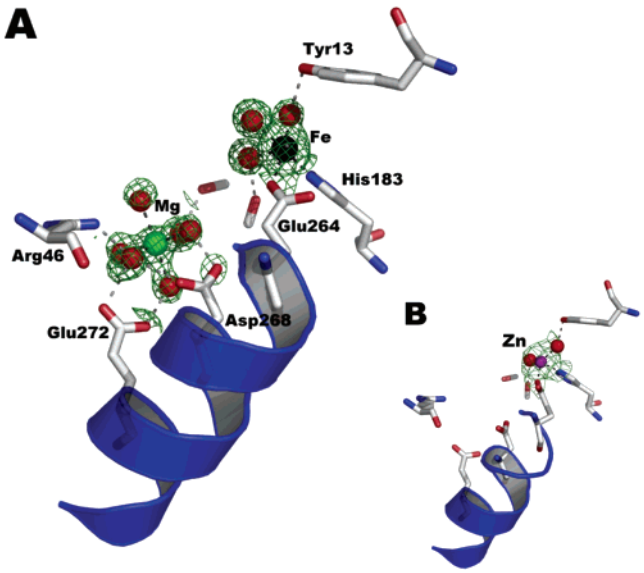

FIGURE 3: Comparison between the iron structure (A) and zinc structure (B), showing the amino acid residue coordination in the active site. The amino acid residue ligands are identical for the two ions. The Zn(II) had a distorted tetrahedral geometry while the iron had a square pyramidal geometry. The Mg(II) that is essential for crystal formation remains in the iron structure but is pushed out by Zn(II). In green, a SIGMAA-weighted ($3F_{obs} - 2F_{calc}$) electron density map for Fe and Mg(II) is contoured at 1σ. The figure was prepared with PyMOL (*47*).

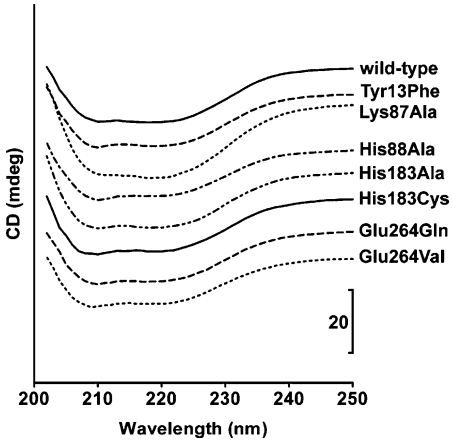

FIGURE 4: CD spectra of wild-type and modified ferrochelatases. The curves overlapped to such an extent that they had to be separated to be comparable. The similar shapes of all the curves indicated the same proportions of secondary elements in the ferrochelatase structures.

higher mobility (the *B* value was 28.54 Å^2 for the water bridging Tyr13 compared to 17.05 Å^2 and 22.09 Å^2 for the other water ligands) (Figure 3). The occupancy of the iron was refined to 87%. The metal could also be seen in a calculated anomalous Bijvoet difference Fourier electron density map up to the 24σ level. At the X-ray wavelength used during data collection (1.06 Å) the contributions from the anomalous scattering factors for iron are $f' = 0.2257$e and $f'' = 1.7432$e. This should be compared with $f' = 0.1008$e and $f'' = 0.0852$e for magnesium. Thus it is clear that the anomalous contribution stems from bound iron. The oxidation state of the iron could not be determined. However, the solubility of Fe(II) and Fe(III) hydroxide at pH 8.5 (the pH of the crystallization buffer) is $<5 \times 10^{-6}$ M and $<9 \times 10^{-23}$ M, respectively. Therefore, the iron is most likely in the Fe(II) state when it binds to ferrochelatase, but it may be oxidized to Fe(III) once in the active site as the soaking procedure was carried out aerobically. The previously mentioned soaking procedures that employed Fe(II) solutions failed because precipitation of Fe(III) began immediately when the solution was exposed to oxidizing conditions. It should be noted that it is Fe(II), not Fe(III), that is the substrate of ferrochelatase (*44*) and that the Fe(II) state could have been stabilized by the enzyme.

The three remaining irons were found at three sites (Figure 2II−IV). At these sites each iron was coordinated in an octahedral manner and each coordinated by either one or two amino acid residue ligands. These residues were all nonconserved and have never been observed to coordinate metal ions in previous soaking experiments. The occupancies of iron at these sites were also lower than that of the metal at the active site: 63%, 55%, and 37% for site II, III, and IV, respectively.

Three Mg(II) ions were also observed in the iron−ferrochelatase complex structure. One Mg(II) ion with 96% occupancy was found at a site approximately 8 Å away from the iron in the active site (Figure 3). The same site has been described earlier as a Mg(II) binding site, and it is referred to as the outer metal binding site (*11*, *28*, *30*). The function of a metal at this site is not fully understood, but it has been suggested that it has a role in catalysis. A metal at this site has also been observed in the structures of human ferrochelatase (*1*). In the present study the coexistence of Mg(II) and iron at these two sites was notable, as previous studies with Zn(II) have indicated that the two metal ion binding sites cannot be simultaneously occupied (*28*, *30*).

Crystallization was also used to evaluate the structural rearrangements following the various exchanges of amino acid residues. The ferrochelatase variants Tyr13Phe and His183Cys have been crystallized previously (*17*). In this work, we obtained crystals of ferrochelatase variants with His183Ala, His88Ala, and Lys87Ala modifications. However, compared to the wild-type ferrochelatase crystals, those of the His88Ala variant displayed a high degree of mosaicity and twinning, which precluded a reliable refinement, i.e., crystallographic data were obtained for five out of the eight modified ferrochelatases used in the present study. To indicate the structural integrity of the remaining ferrochelatase variants, Glu264Val, Glu264Gln, and His88Ala, CD spectroscopy was used. The spectral variations of the group were not significantly different from that of the ferrochelatase variants for which crystallographic data were obtained, indicating a native and functional fold of all enzymes (Figure 4).

The affinity estimations suggested His183 and Glu264 to be the determining metal binding residues. However, only crystallization of His183 variants was successful. After the addition of $(NH_4)_2Fe(SO_4)_2 \cdot 6H_2O$ to a His183Ala crystal no iron was observed in the active site. However, an iron was still present at site II, coordinated by the same residue His201. This site had the second highest occupancy in the soaking of the wild-type protein. This ensured that the soaking procedure had worked.

The ferrochelatase with a Lys87Ala modification diffracted to a high resolution of 1.2 Å, which allowed for the

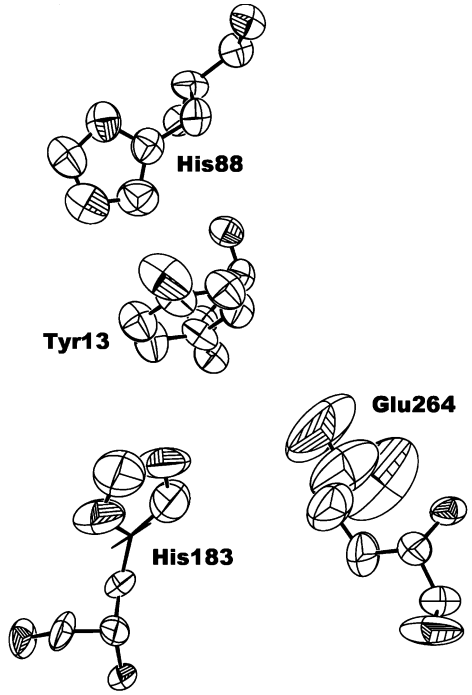

FIGURE 5: ADP of active site residues, based on the 1.2 Å structure of the Lys87Ala modified ferrochelatase, are visualized by thermal ellipsoids. The figure was prepared with PLATON (*48*).

refinement of anisotropic displacement parameters (ADP) using SIMU restraints in SHELXL-97 (*37*). The restraints are based on the assumption that displacements of spatially close atoms will have similar amplitudes and similar directions. The anisotropic refinement of ADP reduced R_{free} by 3.4%. Interestingly, the thermal ellipsoids of the active site residues showed that the carboxyl group of Glu264 undergoes the largest movement (Figure 5), which may be important in substrate binding. The Lys87Ala ferrochelatase structure also displayed the largest root-mean-square deviations (rmsd) in the C-α atom position, compared to the wild-type enzyme. Lys87 is exposed to solvent, and the changes in protein structure affect interactions with neighboring molecules in the crystal. The largest conformational change in the protein involved the upper part of the porphyrin binding cleft (amino acid residues 14−58) and resulted in a more open conformation of the cleft. The side chain of Tyr26 undergoes one of the largest shifts in residue position (Figure 6). The distance from $Tyr26^{OH}$ to $Glu264^{OE}$ increased from 5.1 to 12.0 Å. A similar shift in the position of Tyr26 has previously been observed in the complex of ferrochelatase with *N*-MeMP (*11*). It was suggested that the shift in the position of Tyr26 is essential for the regulation of the conformation of ferrochelatase. The change in position subsequently affects the pK_a value of Glu264, increasing it from 3.25 in wild-type to 4.51 in the Lys87Ala variant. Hence, the properties of Glu264 as a metal binding residue are affected. This may be reflected in the lower affinity of this ferrochelatase variant toward metal, as described above. The lower metal binding affinity of Glu264 in this conformation may be one of the factors contributing to the increase in the ligand exchange rate of the metal upon porphyrin binding (*17*). This may also explain why the activity of the enzyme is not notably affected by this modification.

DISCUSSION

The nature of the catalytic metal binding site in ferrochelatase has been a subject of discussions ever since Dailey first suggested a site in 1984 (*45*). Extensive site-directed mutagenesis studies have been performed and a variety of spectroscopic techniques have been employed in the search for the metal binding residues. However, once the ferrochelatase−*N*-MeMP complex structure had been solved, the discussion focused on two possible sites, suggesting that the metal ion may enter the porphyrin either via His183 and Glu264 (*11*, *28*) or via His88 and Lys87 (*21*). The change in activity following a change in metal binding properties presented in this study strongly supports the suggestion that the metal ion binds to the conserved residues His183 and Glu264, and most probably is inserted into the porphyrin from this site. Thus, the K_d estimates show that the His183Ala and His183Cys modifications significantly altered the affinity for Zn(II) in solution, while modifications of Tyr13 and His88, located in the vicinity of the metal binding site, did not have a significant effect on metal binding. The role of His183 in metal binding is also supported by the low activity of the His183Cys variant, which is probably a result of a high metal binding affinity of the cysteine. A metal binding role for His183 is further supported by previous studies with the His183Cys variant, which showed a reduced rate of Cu(II) insertion into *N*-MeMP by quantitative mass spectrometry (*17*). It is possible that the metal binding capacity of the Glu264Val ferrochelatase had been almost completely eliminated, as no reliable K_d could be determined. In contrast, the Glu264Gln variant retained a high affinity for Zn(II), which may be explained by the polar character of the glutamine side chain. The decrease in metal binding affinity of the Lys87Ala variant of the enzyme is probably a result of a shift in the position of Tyr26, which (as noted above) may have implications for the reaction mechanism of the enzyme.

In this study, X-ray crystallography revealed that the iron in the active site was coordinated by the same amino acid residues as Zn(II), both in the first and in the second coordination sphere. The nature of the iron ligands observed in this work is consistent with previous EXAFS studies that have indicated a penta- or hexacoordinated species with only nitrogen or oxygen ligands, two to three of which have been solvent molecules (*27*). The fact that binding of iron and Zn(II) employs the same protein ligands also justifies the many studies that have used zinc in assays of the ferrochelatase reaction. Unfortunately there is no available structure of ferrochelatase in complex with iron and a porphyrin available. However, the present structure of a ferrochelatase containing iron can provide insight into the path of the metal into the active site of the enzyme. In a theoretical study, it has been suggested that the metal−nitrogen bond formations are facilitated by dehydration and decrease in the coordination number of the Fe(II) upon binding to ferrochelatase (*16*). The octahedral configuration of the Mg(II) ligands at the site next to the iron has previously been suggested to provide an initial metal binding site (*28*). Upon movement into the active site the metal is dehydrated and adopts a catalytically more favorable configuration. A superposition of the wild-type iron−ferrochelatase structure onto the *N*-MeMP cocrystallized structure showed that if iron binding is to occur

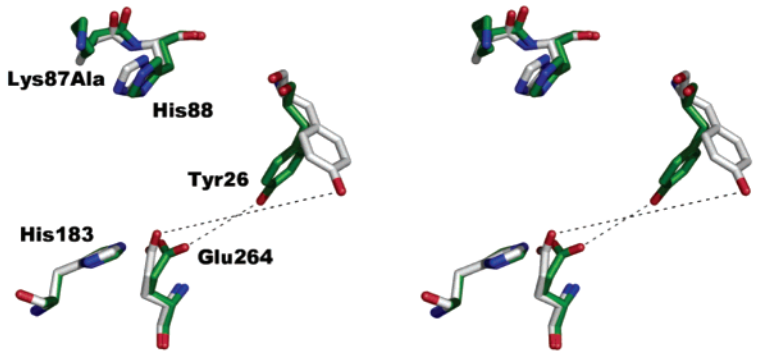

FIGURE 6: Stereoview of the superimposed structures of wild-type (in green) and Lys87Ala (in gray) ferrochelatases showing the rearrangement of Tyr26 relative to Glu264 following the replacement of Lys87 by Ala. The rearrangement increases the pK_a of Glu264 and hence affects its metal binding properties. The figure was prepared with PyMOL (*47*).

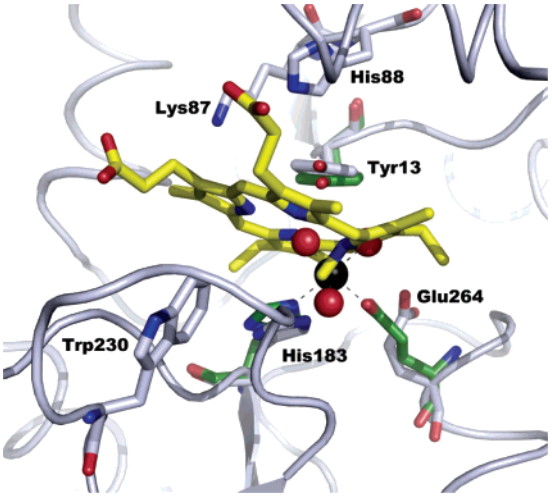

FIGURE 7: Superposition of the active site with bound Fe ion in wild-type ferrochelatase (green with Fe in black and water ligands in red) onto the cocrystal structure of *N*-MeMP and ferrochelatase (PDB code 1C1H) (gray with *N*-MeMP yellow). The figure was prepared with PyMOL (*47*).

in the manner described in the present study, two additional solvent molecules need to be removed or displaced (Figure 7). Interestingly, these two solvent molecules occupy positions that essentially coincide with the position of the nitrogen atoms of pyrrole rings A and B. Also, the temperature factor of the water molecule that interacts with Tyr13 is rather high, which indicates a weaker binding.

The formation of heme cannot be completed until the metalated porphyrin has been deprotonated. It has been suggested that the deprotonation should occur at a site opposite to the metal binding site (*16*, *21*). The reaction is slow with a turnover that is 24 min^{-1} for the purified *B. subtilis* ferrochelatase and 0.2 min^{-1} in exponentially growing *B. subtilis* cells (*13*). Therefore, a water molecule may be as suitable a proton acceptor as an amino acid residue. Nevertheless, theoretical calculations favor the involvement of an amino acid residue for proton removal (*16*). A His88Ala modification in ferrochelatase had a significant effect on enzyme activity even though it retained wild-type metal affinity. If metal insertion and proton abstraction occurs on opposite sides, this could indicate a role for His88 in the deprotonation of the metalated porphyrin by *B. subtilis* ferrochelatase. However, His88 is nonconserved and further experiments are required to reveal the deprotonation step in the ferrochelatase reaction.

REFERENCES

1. Dailey, H. A., and Dailey, T. A. (2003) Ferrochelatase, in *Porphyrin handbook: The Iron and Cobalt Pigments: Biosynthesis, Structure and Degradation* (Kadish, K. M., Smith, K. M., and Guilard, R., Eds.) pp 93−122, Academic Press, San Diego.
2. Kaim, W., and Schwederski, B. (1994) *Bioinorganic chemistry: Inorganic elements in the chemistry of life: An introduction and guide*, John Wiley & Sons, Chichester.
3. Shima, S., Sordel-Klippert, M., Brioukhanov, A., Netrusov, A., Linder, D., and Thauer, R. K. (2001) Characterization of a heme-dependent catalase from *Methanobrevibacter arboriphilus*, *Appl. Environ. Microbiol. 67*, 3041−3045.
4. Badminton, M. N., and Elder, G. H. (2005) Molecular mechanisms of dominant expression in porphyria, *J. Inherited Metab. Dis. 28*, 277−286.
5. Fuchs, J., Weber, S., and Kaufmann, R. (2000) Genotoxic potential of porphyrin type photosensitizers with particular emphasis on 5-aminolevulinic acid: implications for clinical photodynamic therapy, *Free Radical Biol. Med. 28*, 537−548.
6. Granville, D. J., McManus, B. M., and Hunt, D. W. (2001) Photodynamic therapy: shedding light on the biochemical pathways regulating porphyrin-mediated cell death, *Histol. Histopathol. 16*, 309−317.
7. Cochran, A. G., and Schultz, P. G. (1990) Antibody-catalyzed porphyrin metallation, *Science 249*, 781−783.
8. Yin, J., Beuscher, A. E., IV, Andryski, S. E., Stevens, R. C., and Schultz, P. G. (2003) Structural plasticity and the evolution of antibody affinity and specificity, *J. Mol. Biol. 330*, 651−656.
9. Conn, M. M., Prudent, J. R., and Schultz, P. G. (1996) Porphyrin metalation catalyzed by a small RNA molecule, *J. Am. Chem. Soc. 118*, 7012−7013.
10. Li, Y., and Sen, D. (1996) A catalytic DNA for porphyrin metallation, *Nat. Struct. Biol. 3*, 743−747.
11. Lecerof, D., Fodje, M., Hansson, A., Hansson, M., and Al-Karadaghi, S. (2000) Structural and mechanistic basis of porphyrin metallation by ferrochelatase, *J. Mol. Biol. 297*, 221−232.
12. Al-Karadaghi, S., Franco, R., Hansson, M., Shelnutt, J. A., Isaya, G., and Ferreira, G. C. (2006) Chelatases: distort to select?, *Trends Biochem. Sci. 31*, 135−142.
13. Hansson, M., and Hederstedt, L. (1994) Purification and characterisation of a water-soluble ferrochelatase from *Bacillus subtilis*, *Eur. J. Biochem. 220*, 201−208.
14. Camadro, J. M., Ibraham, N. G., and Levere, R. D. (1984) Kinetic studies of human liver ferrochelatase. Role of endogenous metals, *J. Biol. Chem. 259*, 5678−5682.
15. Tapiero, H., and Tew, K. D. (2003) Trace elements in human physiology and pathology: zinc and metallothioneins, *Biomed. Pharmacother. 57*, 399−411.
16. Shen, Y., and Ryde, U. (2005) Reaction mechanism of porphyrin metallation studied by theoretical methods, *Chem. Eur. J. 11*, 1549−1564.
17. Shipovskov, S., Karlberg, T., Fodje, M., Hansson, M. D., Ferreira, G. C., Hansson, M., Reimann, C. T., and Al-Karadaghi, S. (2005) Metallation of the transition-state inhibitor *N*-methyl mesoporphyrin by ferrochelatase: implications for the catalytic reaction mechanism, *J. Mol. Biol. 352*, 1081−1090.
18. Inamo, M., Kamiya, N., Inada, Y., Nomura, M., and Funahashi, S. (2001) Structural characterization and formation kinetics of

sitting-atop (SAT) complexes of some porphyrins with copper(II) ion in aqueous acetonitrile relevant to porphyrin metalation mechanism. Structures of aquacopper(II) and Cu(II)-SAT complexes as determined by XAFS spectroscopy, *Inorg. Chem. 40*, 5636−5644.
19. Kohno, H., Okuda, M., Furukawa, T., Tokunaga, R., and Taketani, S. (1994) Site-directed mutagenesis of human ferrochelatase: identification of histidine-263 as a binding site for metal ions, *Biochim. Biophys. Acta 1209*, 95−100.
20. Gora, M., Grzybowska, E., Rytka, J., and Labbe-Bois, R. (1996) Probing the active-site residues in *Saccharomyces cerevisiae* ferrochelatase by directed mutagenesis. In vivo and in vitro analyses, *J. Biol. Chem. 271*, 11810−11816.
21. Sellers, V. M., Wu, C. K., Dailey, T. A., and Dailey, H. A. (2001) Human ferrochelatase: characterization of substrate-iron binding and proton-abstracting residues, *Biochemistry 40*, 9821−9827.
22. Al-Karadaghi, S., Hansson, M., Nikonov, S., Jönsson, B., and Hederstedt, L. (1997) Crystal structure of ferrochelatase: the terminal enzyme in heme biosynthesis, *Structure 5*, 1501−1510.
23. Wu, C. K., Dailey, H. A., Rose, J. P., Burden, A., Sellers, V. M., and Wang, B. C. (2001) The 2.0 Å structure of human ferrochelatase, the terminal enzyme of heme biosynthesis, *Nat. Struct. Biol. 8*, 156−160.
24. Karlberg, T., Lecerof, D., Gora, M., Silvegren, G., Labbe-Bois, R., Hansson, M., and Al-Karadaghi, S. (2002) Metal binding to *Saccharomyces cerevisiae* ferrochelatase, *Biochemistry 41*, 13499−13506.
25. Schubert, H. L., Raux, E., Wilson, K. S., and Warren, M. J. (1999) Common chelatase design in the branched tetrapyrrole pathways of heme and anaerobic cobalamin synthesis, *Biochemistry 38*, 10660−10669.
26. Franco, R., Moura, J. J., Moura, I., Lloyd, S. G., Huynh, B. H., Forbes, W. S., and Ferreira, G. C. (1995) Characterization of the iron-binding site in mammalian ferrochelatase by kinetic and Mössbauer methods, *J. Biol. Chem. 270*, 26352−26357.
27. Ferreira, G. C., Franco, R., Mangravita, A., and George, G. N. (2002) Unraveling the substrate-metal binding site of ferrochelatase: an X-ray absorption spectroscopic study, *Biochemistry 41*, 4809−4818.
28. Lecerof, D., Fodje, M. N., Alvarez León, R., Olsson, U., Hansson, A., Sigfridsson, E., Ryde, U., Hansson, M., and Al-Karadaghi, S. (2003) Metal binding to *Bacillus subtilis* ferrochelatase and interaction between metal sites, *J. Biol. Inorg. Chem. 8*, 452−458.
29. Hansson, M., and Al-Karadaghi, S. (1995) Purification, crystallization, and preliminary X-ray analysis of *Bacillus subtilis* ferrochelatase, *Proteins 23*, 607−609.
30. Hansson, M. D., Lindstam, M., and Hansson, M. (2006) Crosstalk between metal ions in *Bacillus subtilis* ferrochelatase, *J. Biol. Inorg. Chem. 11*, 325−333.
31. GraphPad Prism 4 (2003). GraphPad Software, San Diego, CA.
32. Cerenius, Y., Ståhl, K., Svensson, L., Ursby, T., Oskarsson, Å., Albertsson, J., and Liljas, A. (2000) The crystallography beamline I711 at MAX II, *J. Synchrotron Radiat. 7*, 203−208.
33. Ursby, T., Mammen, C., Cerenius, Y., Svensson, C., Sommarin, B., Fodje, M., Kvick, Å., Logan, D., Als-Nielsen, J., Thunnissen, M., Larsen, S., and Liljas, A. (2004) The new macromolecular crystallography stations at MAX-lab: The MAD station, *AIP Conf. Proc. 705*, 1241−1246.
34. Mammen, C., and Ursby, T. (2004) Bent diamond crystals and multilayer based optics at the new 5-station protein crystallography beamline 'Cassiopeia' at MAX-lab, *AIP Conf. Proc. 705*, 808−811.
35. Kabsch, W. (1993) Automatic processing of rotation diffraction data from crystals of initially unknown symmetry and cell constants, *J. Appl. Crystallogr. 26*, 795−800.
36. Brunger, A. T., Adams, P. D., Clore, G. M., DeLano, W. L., Gros, P., Grosse-Kunstleve, R. W., Jiang, J. S., Kuszewski, J., Nilges, M., Pannu, N. S., Read, R. J., Rice, L. M., Simonson, T., and Warren, G. L. (1998) Crystallography & NMR system: A new software suite for macromolecular structure determination, *Acta Crystallogr. D Biol. Crystallogr. 54*, 905−921.
37. Sheldrick, G. M., and Schneider, T. R. (1997) SHELXL: high-resolution refinement, *Methods Enzymol. 277*, 319−343.
38. Jones, T. A., Zou, J. Y., Cowan, S. W., and Kjeldgaard. (1991) Improved methods for building protein models in electron density maps and the location of errors in these models, *Acta Crystallogr. A 47*, 110-119.
39. Gordon, J. C., Myers, J. B., Folta, T., Shoja, V., Heath, L. S., and Onufriev, A. (2005) H++: a server for estimating pK_as and adding missing hydrogens to macromolecules, *Nucleic Acids Res. 33*, W368−W371.
40. Bashford, D., and Karplus, M. (1990) pK_a's of ionizable groups in proteins: atomic detail from a continuum electrostatic model, *Biochemistry 29*, 10219−10225.
41. Berg, J. M., and Shi, Y. (1996) The galvanization of biology: a growing appreciation for the roles of zinc, *Science 271*, 1081−1085.
42. Hashimoto, Y., Yamashita, M., and Murooka, Y. (1997) The *Propionibacterium freudenreichii hemYHBXRL* gene cluster, which encodes enzymes and a regulator involved in the biosynthetic pathway from glutamate to protoheme, *Appl. Microbiol. Biotechnol. 47*, 385−392.
43. Cole, S. T., Brosch, R., Parkhill, J., Garnier, T., Churcher, C., Harris, D., Gordon, S. V., Eiglmeier, K., Gas, S., Barry, C. E., 3rd, Tekaia, F., Badcock, K., Basham, D., Brown, D., Chillingworth, T., Connor, R., Davies, R., Devlin, K., Feltwell, T., Gentles, S., Hamlin, N., Holroyd, S., Hornsby, T., Jagels, K., Krogh, A., McLean, J., Moule, S., Murphy, L., Oliver, K., Osborne, J., Quail, M. A., Rajandream, M. A., Rogers, J., Rutter, S., Seeger, K., Skelton, J., Squares, R., Squares, S., Sulston, J. E., Taylor, K., Whitehead, S., and Barrell, B. G. (1998) Deciphering the biology of *Mycobacterium tuberculosis* from the complete genome sequence, *Nature 393*, 537−544.
44. Dailey, H. A. (1990) Conversion of coproporphyrinogen to protoheme in higher eukaryotes and bacteria: terminal three enzymes, in *Biosynthesis of heme and chlorophylls* (Dailey, H. A., Ed.) pp 125-161, McGraw-Hill Publishing Co., New York.
45. Dailey, H. A. (1984) Effect of sulfhydryl group modification on the activity of bovine ferrochelatase, *J. Biol. Chem. 259*, 2711−2715.
46. Studier, F. W., and Moffatt, B. A. (1986) Use of bacteriophage T7 RNA polymerase to direct selective high-level expression of cloned genes, *J. Mol. Biol. 189*, 113−130.
47. DeLano, W. L. (2004) Open-Source PyMOL. DeLano Scientific LLC, San Carlos, CA.
48. Spek, A. L. (2003) Single-crystal structure validation with the program PLATON, *J. Appl. Crystallogr. 36*, 7−13.

BI061760A